



Rapid Radical–Radical Induced Explosive Desorption of Ice-coated Interstellar Nanoparticles

Cheng Zhu^{1,2} , Alexandre Bergantini^{1,2,3} , Santosh K. Singh^{1,2}, Matthew J. Abplanalp^{1,2}, and Ralf I. Kaiser^{1,2} 

¹Department of Chemistry, University of Hawaii at Mānoa, Honolulu, HI 96822, USA; ralfk@hawaii.edu

²W.M. Keck Laboratory in Astrochemistry, University of Hawaii at Mānoa, Honolulu, HI 96822, USA

Received 2021 February 12; revised 2021 June 1; accepted 2021 July 3; published 2021 October 15

Abstract

The observation of complex organic molecules (COMs) in the gas phase of cold molecular clouds has coined a freeze-out paradox in astrophysics: COMs should be accreted on low-temperature interstellar grains, but not observable in cold molecular clouds. Still, validated mechanisms transporting molecules from the grains back into the gas phase are still elusive, but critical for our understanding of the chemical evolution of the molecular universe. Here we report on the first characterization of rapid radical reactions involving methyl (CH₃) and formyl (HCO) radicals in interstellar analogous ices of methane (CH₄) and carbon monoxide (CO) upon exposure to proxies of galactic cosmic rays. Rapid radical chain reactions and explosive desorption occurred once the accumulated radicals surpassed critical concentrations of about 1% in the ices at temperatures of cold molecular clouds (5–10 K). These processes may explain the ejection and observation of COMs in the gas phase of cold molecular clouds and potentially rapid outbursts of comets.

Unified Astronomy Thesaurus concepts: [Laboratory astrophysics \(2004\)](#); [Interstellar molecules \(849\)](#); [Radical-radical recombination \(1071\)](#); [Molecule formation \(2076\)](#); [Astrochemistry \(75\)](#)

1. Introduction

Since the detection of complex organic molecules (COMs)—organics containing several atoms of carbon, hydrogen, nitrogen, and oxygen—such as acetaldehyde (CH₃CHO), methyl formate (HCOOCH₃), and dimethyl ether (CH₃OCH₃) in the gas phase of cold molecular clouds like the Taurus Molecular Cloud 1 (TMC-1) (Table A1) (Rank et al. 1971; Herbst & Klemperer 1973), astronomers and physical chemists have been puzzled by the freeze-out paradox that COMs should not exist in the gas phase because at temperatures typical of cold molecular clouds (10–20 K), they should have been frozen onto the interstellar grains. Gas-phase processes synthesizing mostly saturated COMs in molecular clouds through complex networks of ion–molecule reactions (Herbst & Klemperer 1973), dissociative ion–electron recombination (Geppert et al. 2006), and neutral–neutral reactions (Vasyunina et al. 2013) have been proposed to account for their gas-phase presence (Garrod et al. 2006), but astrochemical models do not match the astronomical observations and severely under-reproduce their fractional abundances by up to three orders of magnitude (Garrod et al. 2006). Recent simulations reproducing COM abundances exhibit better agreement with observations by taking into account of grain chemical processes and reactive desorption but there are still discrepancies for few species (Vasyunin & Herbst 2013). Therefore, the existence of COMs in the gas phase at such low temperatures still represents a fundamental enigma in astrophysics, revealing that hitherto elusive mechanisms must exist that return molecules accreted on the grains back into space, thus preventing the complete removal of COMs from the gas phase in cold molecular clouds.

Several processes have been proposed to explain how COMs might have been replenished into the gas phase from icy grains (d’Hendecourt et al. 1982; Johnson et al. 1991; Roberts et al. 2007; Vasyunin & Herbst 2013; Bludov et al. 2020; Fredon et al. 2021).

First, an advocated photon desorption of COMs, which is efficient at the edges of clouds (Willacy & Millar 1998), is negligible in their interior due to the absorption and scattering of ultraviolet (UV) photons by dust (Tielens & Hagen 1982; d’Hendecourt et al. 1985). A second hypothesis focuses on galactic cosmic rays (GCRs) since high-energy GCRs are able to penetrate deep into dense regions and induce sputtering of frozen molecules (De Barros et al. 2014; Dartois et al. 2019, 2021). Heavy ions in the GCRs, which account for about 1% of the particle component (Johnson et al. 1991), generate an internal UV photon field (Hartquist & Williams 1990) that induces secondary UV radiation and subsequent photodesorption (Öberg et al. 2009b, 2009c; Fayolle et al. 2011; Bertin et al. 2016), lead to impulsive grain heating (Willacy & Millar 1998), and trigger the formation of reactive radicals inside the icy grain mantles. Although laboratory studies reveal that UV photons and spot heating are able to eject solid organics into the gas phase, modeling of fractional abundances requires combination with other desorption mechanisms to replicate the astronomical observations of the detected species quantitatively (Kalvāns 2015). Third, desorption can be induced by the energy released from chemical reactions, e.g., HCO + H → CO + H₂, H₂CO + H → HCO + H₂ (Minissale & Dulieu 2014; Minissale et al. 2016a, 2016b). Fourth, chemical explosive desorption mechanisms governed by a rapid ejection of accreted molecules through the release of “chemical energy” from the reactions of radicals stored in the ice mantles have been offered as a promising alternative (d’Hendecourt et al. 1982; Schutte & Greenberg 1991; Roberts et al. 2007; Vasyunin & Herbst 2013). d’Hendecourt et al. photolyzed interstellar analogous ices of, e.g., carbon monoxide (CO), methane (CH₄), ammonia (NH₃), and water (H₂O) at 10 K using UV light and observed sudden luminescence and pressure surges during the warm-up of the ices, with the main explosive events occurring close to 27 K, i.e., the sublimation temperature of carbon monoxide (CO) under thermal equilibrium conditions (d’Hendecourt et al. 1982). Schutte et al. noticed similar phenomena while annealing photolyzed ices of water (H₂O), carbon monoxide (CO), and ammonia (NH₃),

³ Present address: Centro Federal de Educacao Tecnologica Celso Suckow da Fonseca—CEFET/RJ, Av. Maracana 229, 20271-110, Rio de Janeiro, Brazil.

suggesting that up to 60% of the material can be ejected upon heating (Schutte & Greenberg 1991). Later experiments identified hydrogen (H_2) bursts accompanied by an ejection of up to 90% of solid samples during irradiation of methane ices by 9.0 MeV α particles (He^{2+}) and 7.3 MeV protons (H^+) at 10 K *without* annealing the sample (Kaiser et al. 1997). Energetic electrons—formed in the track of GCRs penetrating interstellar ices—processing methane ices also induced a rapid emission of molecules into the gas phase accompanied by luminescence flashes even close to 4.7 K after reaching critical irradiation doses of 6.25 eV amu^{-1} (Savchenko et al. 2019, 2020). These results suggest a GCR-triggered generation of radicals, which accumulate in interstellar (model) ices at temperatures of 5–10 K in cold molecular clouds; critical radical concentrations of up to a few percent induce rapid, radical–radical reactions accompanied by an “explosive” ejection of organic matter into the gas phase (Johnson et al. 1991; Roberts et al. 2007; Vasyunin & Herbst 2013). However, a (spectroscopic) tracing of these radical reactions at ultralow temperatures and radiation doses representing molecular clouds has not been reported to date.

In this article, we present the very first direct observation of rapid radical–radical reactions of formyl ($\text{HCO}\bullet$) and methyl ($\bullet\text{CH}_3$) radicals along with hydrogen atoms and the reaction-induced explosive desorption during the exposure of apolar interstellar model ices of methane and carbon monoxide to ionizing radiation in form of 5 keV electrons (Bennett & Kaiser 2007; Abplanalp et al. 2016; Turner et al. 2018) at temperatures as low as 5 K. These experiments mimic the processing of interstellar ices by secondary electrons released when GCRs penetrate icy grains (see the Appendix) (Yeghikyan 2011). Apolar model ices under anhydrous conditions were chosen to explore the proof-of-concept and the temperature dependence of rapid reactions among open-shell species. Carbon monoxide and methane have been identified toward multiple high-mass star-forming regions at levels of up to 80% and 11%, respectively (Boogert et al. 2015). An elucidation of these mechanisms is imperative not only to constrain the fundamental processes, which trigger rapid radical–radical reactions at ultralow temperatures within interstellar grains, but also to objectively evaluate the hitherto elusive role of these processes in the transfer of COMs formed throughout ice-coated interstellar grains into the gas phase of cold molecular clouds, even at 10 K, thus eventually expanding our knowledge of the enigmatic cycling of organics between the gas phase and interstellar icy grains in our universe.

2. Experimental Procedures

The experiments were carried out in an ultrahigh-vacuum chamber (1×10^{-10} Torr) by exposing ice mixtures of methane and carbon monoxide to energetic electrons (5 keV, 30 nA) at low temperatures (5–20 K) (Appendix, Tables A2 and A3). During the irradiation, the chemical evolution of the ices was monitored online and in situ via Fourier transform infrared (FTIR) spectroscopy. The molecules in the gas phase were detected using a quadrupole mass spectrometer (QMS). After the irradiation, the ices were warmed to 300 K at a rate of 1 K min^{-1} (temperature-programmed desorption, TPD). During the TPD phase, any subliming molecules were monitored by exploiting a tunable vacuum ultraviolet (VUV) photoionization (PI) reflectron time-of-flight mass spectrometer (PI-ReTOF-MS) (Table A4).

3. Results and Discussion

3.1. Infrared Spectroscopy

FTIR spectroscopy represents a universal tool not only to characterize small molecules and radicals in situ, but also to monitor the chemical evolution of the radicals in methane–carbon monoxide model ices during electron irradiation at characteristic temperatures of molecular clouds from 5 to 20 K (Tables A2 and A3). In the 5 K experiment, the exposure of the ices to ionizing radiation led to the decomposition of the precursors and to a *gradual* formation of new absorptions of methyl ($\bullet\text{CH}_3$, 3153 cm^{-1}), ethane (C_2H_6 , 2979 cm^{-1}), carbon dioxide (CO_2 , 2341 cm^{-1}), formyl ($\text{HCO}\bullet$, 1853 cm^{-1}), and carbonyl group ($\text{C}=\text{O}$, $1750\text{--}1680 \text{ cm}^{-1}$) (Figures 1 and 2, Table A5) until the irradiation time reached 11 minutes, i.e., a corresponding dose of $0.030 \pm 0.004 \text{ eV amu}^{-1}$. At these low doses, the carriers of the $\text{C}=\text{O}$ bands are predominantly formaldehyde (H_2CO) and acetaldehyde (CH_3CHO) (Kaiser et al. 2014). An absorption at 1351 cm^{-1} was also assigned to CH_3CHO . Thereafter, the concentrations of $\bullet\text{CH}_3$ and $\text{HCO}\bullet$ radicals decreased sharply; this decrease is accompanied by a simultaneous rise in the concentrations of C_2H_6 and $\text{C}=\text{O}$ group and an increase in the chamber pressure (Figures 1 and 2). A QMS (Appendix) monitored sublimation of carbon monoxide and methane during this process, which were calculated to be $(1.9 \pm 0.9) \times 10^{14}$ and $(0.6 \pm 0.3) \times 10^{14}$ molecules, respectively, by comparing their ion counts with those in two calibration experiments using pure CO_2 and CH_4 . The desorbed CO_2 and CH_4 account for close to 0.1% of the molecules in ice. These FTIR and QMS findings imply rapid reactions of the accumulated radicals, forming new organics and inducing explosive desorption.

Having observed explosive desorption induced by rapid radical–radical reactions, we performed a series of experiments to study the effects of irradiation dose, temperature, isotope, and precursors on this phenomenon (Figure 3). The phenomenon was observed again upon further exposure of the ices to ionizing radiation after the electron dose reached $0.096 \pm 0.015 \text{ eV amu}^{-1}$ (Figure 3(A)). A replacement of methane by deuterated methane (CD_4) (Table A6) has a profound effect and delays the radical–radical recombination (Figure 3(B)) with concentrations of the D3-methyl ($\bullet\text{CD}_3$) and D1-formyl ($\text{DCO}\bullet$) leveling off until the irradiation doses reach $0.069 \pm 0.010 \text{ eV amu}^{-1}$ and $0.110 \pm 0.016 \text{ eV amu}^{-1}$. These effects were also observed in the 10 K experiment (Figure 3(C)), but vanished when the experiments were conducted at 15 K and 20 K (Figures 3(D) and (E)), cf. the discussion below. Note that this phenomenon is not limited to methane; in a separate experiment, exploiting ethane (C_2H_6)–carbon monoxide (C^{18}O) model ices, ethyl ($\text{C}_2\text{H}_5\bullet$) and formyl ($\text{HC}^{18}\text{O}\bullet$) radicals also accumulated and were followed by a rapid decrease at a critical dose of $0.053 \pm 0.006 \text{ eV amu}^{-1}$ accompanied by a simultaneous enhancement of carbonyl ($\text{C}=\text{O}$) functional groups (Figure A1 and Table A7).

Having traced the temporal profiles of the radicals and the rapid formation of closed-shell organics at critical doses at 5 K and 10 K, we attempt to untangle the underlying reaction pathways. A reaction scheme was developed to kinetically fit the temporal evolution of the column densities of the observed species during the irradiation (Figure 3(F), Tables 1 and A8). At these low doses, the carbonyl absorptions ($1750\text{--}1680 \text{ cm}^{-1}$) can be satisfactorily accounted for by formaldehyde (H_2CO) and acetaldehyde (CH_3CHO). Upon interaction with the impinging energetic

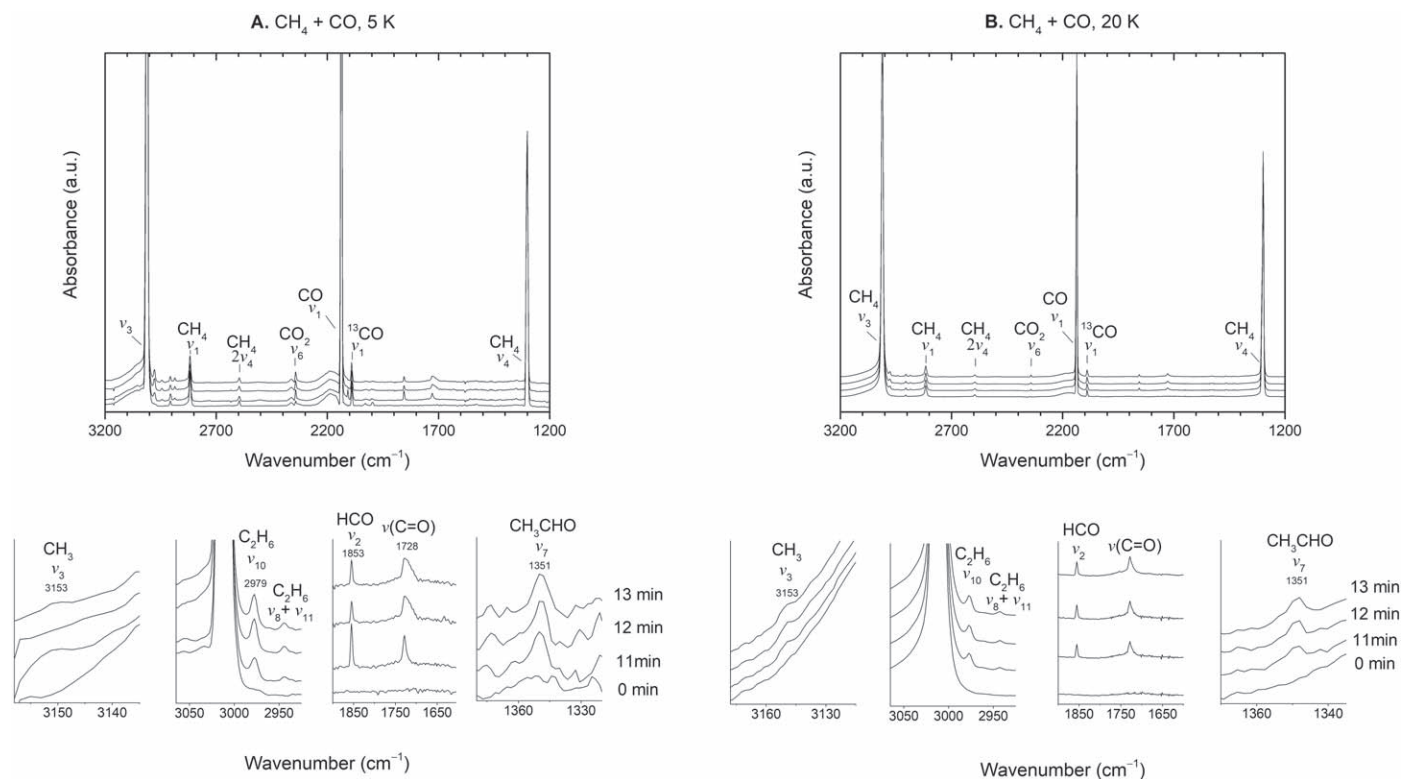


Figure 1. In situ FTIR spectra of methane (CH_4)–carbon monoxide (CO) ices during electron irradiation. FTIR spectra were collected during irradiation (A) at 5 K and (B) at 20 K. For clarity, only significant peaks are labeled; detailed assignments are compiled in Table A5.

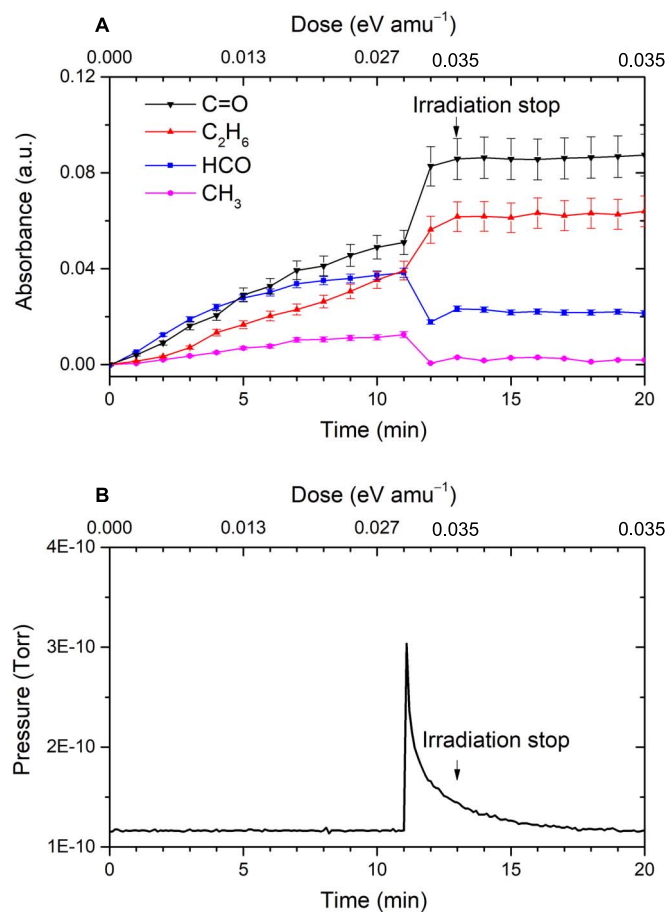


Figure 2. Evolution of (A) infrared absorption and (B) pressure during irradiation.

electrons, methane can undergo cleavage of one of the four chemically equivalent carbon–hydrogen bonds to generate a methyl radical ($\bullet\text{CH}_3$) plus suprathreshold atomic hydrogen ($\text{H}\bullet$) (Reaction (1); Figure 3(F)). Further, two neighboring methane molecules can be converted into an ethane molecule (C_2H_6) plus two suprathreshold hydrogen atoms and/or molecular hydrogen (Reaction (2)) (He et al. 2010). Recombination of two methyl radicals can also lead to ethane (Reaction (3)) if these radicals are in a favorable recombination geometry. The suprathreshold hydrogen atoms released from Reactions (1) and (2) possess excess kinetic energies of a few eV; this energy can be utilized to overcome the entrance barrier (0.11 eV, 11 kJ mol $^{-1}$) (Bennett et al. 2005a) for addition to the carbon monoxide molecule leading to the formyl radical ($\text{HCO}\bullet$) (Reaction (4)). If the formyl radical is formed in a proper geometry for recombination with the previously generated methyl radical (Reaction (1)) and/or atomic hydrogen (Reactions (1) and (2)), these open-shell species can recombine barrierlessly to form acetaldehyde (CH_3CHO , Reaction (5)) and formaldehyde (H_2CO , Reaction (6)), respectively. Based on the aforementioned reactions, the temporal profiles were fit by numerically solving coupled differential reaction rate equations (Table A8) to find reaction rate constants that minimize the sum of the squares of the deviations between calculated and experimental column densities (Frenklach et al. 1992; Bennett et al. 2007). For experiments at 5 and 10 K, these fits divided into five stages: stages 1, 3, and 5 represent the gradual formation of the products, while stages 2 and 4 denote the phase of rapid radical reactions. It is important to note that these results are self-consistent and fully account for the carbon and oxygen budgets in the model ices (Table A9).

Quantitatively speaking, it is interesting to compare the extracted reaction rate constants in distinct systems to unveil the effects of isotope substitution (H versus D) and of the

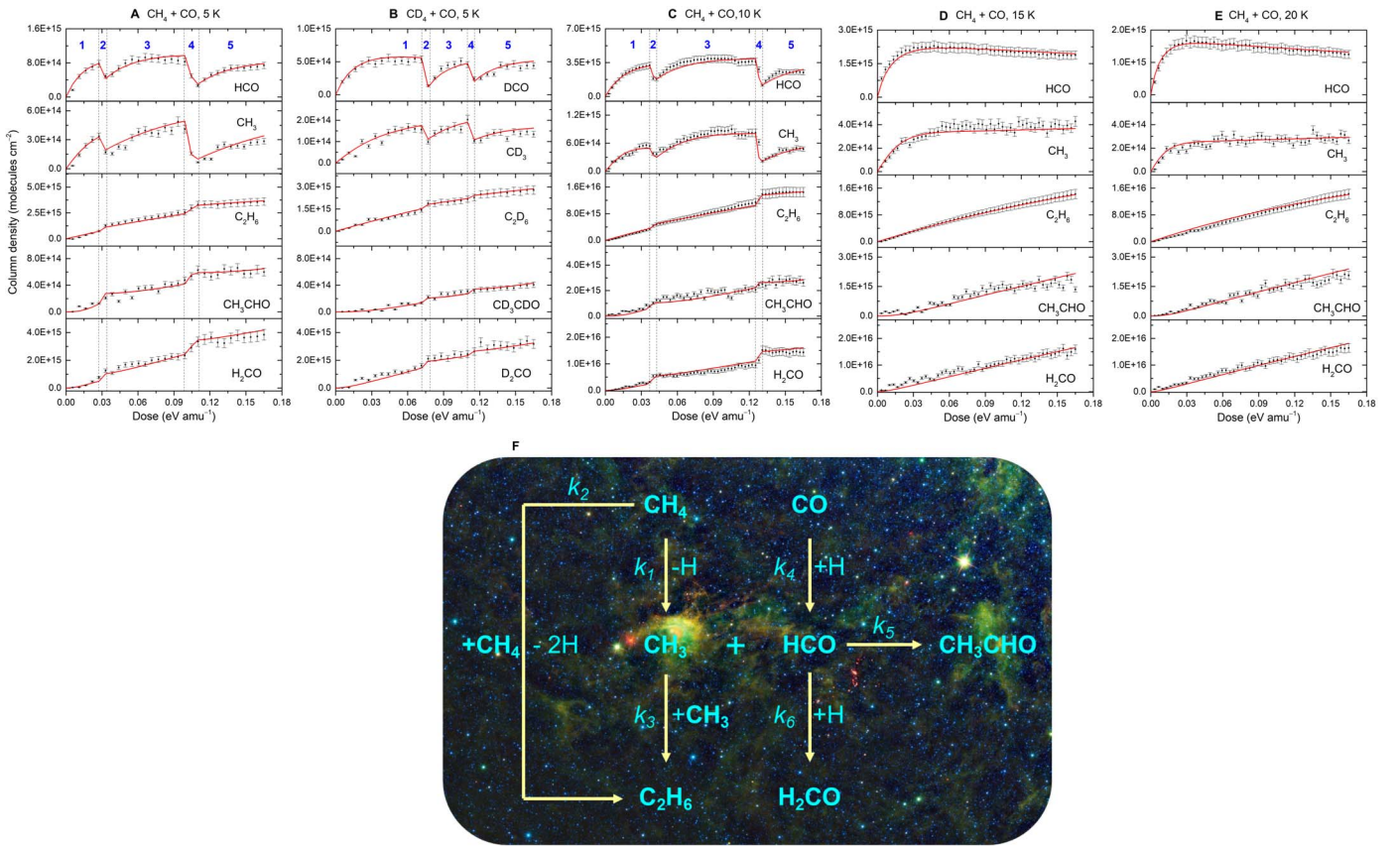


Figure 3. (A)–(E) Temporal profiles of the column densities of key species during irradiation. (F) Reaction scheme used to fit the profiles. The kinetic fits are shown by red lines. Rate constants are compiled in Table 1.

temperature on the radical reactions (Table 1). Note that the atoms and radicals generated by energetic electrons are mostly suprathermal (Morton & Kaiser 2003). Their reactions are not in thermal equilibrium. The collision frequencies of the electrons with the species in the ices also affect reaction rates. Therefore, the extracted rate constants are not independent from the column densities of reactants. In the first stage of the 5 K experiment (CH₄/CO), the rate constants generating •CH₃ (k_1) and HCO• (k_4) radicals were derived to be $(2.96 \pm 0.30) \times 10^{-6} \text{ s}^{-1}$ and $(1.27 \pm 0.13) \times 10^{-18} \text{ cm}^2 \text{ s}^{-1}$, respectively; the rates of consuming •CH₃ and HCO• via Reactions (3) (k_3), (5) (k_5), and (6) (k_6) were found to be $(1.47 \pm 0.15) \times 10^{-19} \text{ cm}^2 \text{ s}^{-1}$, $(1.69 \pm 0.17) \times 10^{-18} \text{ cm}^2 \text{ s}^{-1}$, and $(2.10 \pm 0.21) \times 10^{-16} \text{ cm}^2 \text{ s}^{-1}$, respectively. During the radical–radical reactions (stage 2), the formation rates of •CH₃ and HCO• via Reactions (1) and (4) slightly decreased ($k_1 = (2.75 \pm 0.28) \times 10^{-6} \text{ s}^{-1}$ and $k_4 = (1.23 \pm 0.12) \times 10^{-18} \text{ cm}^2 \text{ s}^{-1}$), but the production rates of ethane, acetaldehyde, and formaldehyde increased by about one order of magnitude ($k_3 = (4.47 \pm 0.45) \times 10^{-18} \text{ cm}^2 \text{ s}^{-1}$, $k_5 = (9.09 \pm 0.91) \times 10^{-18} \text{ cm}^2 \text{ s}^{-1}$, and $k_6 = (8.03 \pm 0.80) \times 10^{-16} \text{ cm}^2 \text{ s}^{-1}$), suggesting that rapid radical Reactions (3)–(5) involving •CH₃, HCO•, and atomic hydrogen occurred. This trend is also reflected in stages 3 and 4. In the final stage 5 the rate constants are slightly lower than the production rates in stages 1 and 3, possibly due to a slow drop of radiolysis efficiency as the precursors were gradually decomposed by energetic electrons. It is important to note that in the CD₄/CO system at 5 K, the reaction rates are noticeably lower than those in the CH₄/CO system, suggesting strong isotopic effects of deuterium that de facto reduce the radical–radical recombination

rates by up to a factor of about four (Table 1). A change of the temperature from 5 to 10 K during the irradiation only marginally affected the rate constants. However, a further increase in the temperature to 15 and 20 K had a dramatic effect on the kinetics and essentially eliminated the five-stage reaction pattern. The formation of •CH₃ (Reaction (1)) is driven by the energetic electron dose and should be independent of ice temperature. Nonetheless, high temperature promotes diffusion of radicals, facilitating reactions of •CH₃ (Reaction (3)) and HCO• (Reactions (5) and (6)), thus essentially decreasing the overall yield of •CH₃ while simultaneously increasing the consumption rates of the radicals. This hypothesis is supported by the fact that k_1 values in the 20 and 15 K experiments are lower than in the 10 and 5 K studies (phases 1, 3, 5), while especially k_3 and also k_5 reveal the opposite trend. This effectively diminishes the capability of the ice to efficiently store radicals at elevated temperatures. Radical concentrations for •CH₃ at 20 K and 15 K did not exceed $(0.09 \pm 0.01)\%$ and $(0.11 \pm 0.01)\%$, respectively. Nevertheless, the •CH₃ radicals reached higher levels of $(0.16 \pm 0.02)\%$ and $(0.29 \pm 0.03)\%$ at 10 K and 5 K, respectively, prior to the rapid radical–radical reactions (Tables A10 and A11).

3.2. PI-ReTOF-MS

To confirm the identification of formaldehyde (H₂CO) and acetaldehyde (CH₃CHO), we heated the electron-processed ice to 300 K (TPD) and exploited PI-ReTOF-MS to monitor the subliming molecules. This unique approach is able to unambiguously identify gas-phase molecules by systematically tuning the photon energies (PEs) above and below the ionization energies

Table 1
All Rate Constants Derived via Iterative Solution to the Proposed Reaction Scheme

Reaction	Temperature	Rate Constant				
		Stage 1	Stage 2	Stage 3	Stage 4	Stage 5
$\text{CH}_4 \rightarrow \text{CH}_3 + \text{H}$ k_1 (in s^{-1})	5 K $\text{CH}_4 + \text{CO}$	$(2.96 \pm 0.30) \times 10^{-6}$	$(2.75 \pm 0.28) \times 10^{-6}$	$(1.36 \pm 0.14) \times 10^{-6}$	$.8(1.28 \pm 0.13) \times 10^{-6}$	$(1.03 \pm 0.10) \times 10^{-6}$
	5 K $\text{CD}_4 + \text{CO}$	$(7.91 \pm 0.80) \times 10^{-7}$	$(7.53 \pm 0.75) \times 10^{-7}$	$(6.20 \pm 0.62) \times 10^{-7}$	$(4.31 \pm 0.43) \times 10^{-7}$	$(3.09 \pm 0.31) \times 10^{-7}$
	10 K $\text{CH}_4 + \text{CO}$	$(2.00 \pm 0.20) \times 10^{-6}$	$(1.91 \pm 0.20) \times 10^{-6}$	$(1.54 \pm 0.16) \times 10^{-6}$	$.8(1.27 \pm 0.13) \times 10^{-6}$	$(1.01 \pm 0.10) \times 10^{-6}$
	15 K $\text{CH}_4 + \text{CO}$			$(1.18 \pm 0.12) \times 10^{-6}$		
	20 K $\text{CH}_4 + \text{CO}$			$(1.23 \pm 0.13) \times 10^{-6}$		
$\text{CH}_4 + \text{CH}_4 \rightarrow \text{C}_2\text{H}_6 + 2\text{H}$ k_2 (in $\text{cm}^2 \text{s}^{-1}$)	5 K $\text{CH}_4 + \text{CO}$	$(1.81 \pm 0.19) \times 10^{-23}$	$(4.81 \pm 0.49) \times 10^{-23}$	$(1.61 \pm 0.17) \times 10^{-23}$	$(4.78 \pm 0.48) \times 10^{-23}$	$(1.11 \pm 0.10) \times 10^{-23}$
	5 K $\text{CD}_4 + \text{CO}$	$(1.58 \pm 0.16) \times 10^{-23}$	$(4.22 \pm 0.43) \times 10^{-23}$	$(1.13 \pm 0.12) \times 10^{-23}$	$(2.81 \pm 0.30) \times 10^{-23}$	$(1.03 \pm 0.10) \times 10^{-23}$
	10 K $\text{CH}_4 + \text{CO}$	$(0.95 \pm 0.10) \times 10^{-24}$	$(2.42 \pm 0.25) \times 10^{-23}$	$(0.74 \pm 0.10) \times 10^{-23}$	$(3.99 \pm 0.40) \times 10^{-23}$	$(0.61 \pm 0.10) \times 10^{-23}$
	15 K $\text{CH}_4 + \text{CO}$			$(1.22 \pm 0.13) \times 10^{-23}$		
	20 K $\text{CH}_4 + \text{CO}$			$(1.28 \pm 0.14) \times 10^{-23}$		
$\text{CH}_3 + \text{CH}_3 \rightarrow \text{C}_2\text{H}_6$ k_3 (in $\text{cm}^2 \text{s}^{-1}$)	5 K $\text{CH}_4 + \text{CO}$	$(1.47 \pm 0.15) \times 10^{-19}$	$(4.47 \pm 0.45) \times 10^{-18}$	$(1.37 \pm 0.14) \times 10^{-19}$	$(1.47 \pm 0.15) \times 10^{-17}$	$(1.37 \pm 0.14) \times 10^{-19}$
	5 K $\text{CD}_4 + \text{CO}$	$(1.27 \pm 0.13) \times 10^{-19}$	$(3.77 \pm 0.38) \times 10^{-18}$	$(1.13 \pm 0.11) \times 10^{-19}$	$(9.91 \pm 0.99) \times 10^{-18}$	$(1.02 \pm 0.10) \times 10^{-19}$
	10 K $\text{CH}_4 + \text{CO}$	$(1.33 \pm 0.13) \times 10^{-19}$	$(2.41 \pm 0.24) \times 10^{-18}$	$(1.30 \pm 0.13) \times 10^{-19}$	$(9.47 \pm 0.95) \times 10^{-18}$	$(1.25 \pm 0.13) \times 10^{-19}$
	15 K $\text{CH}_4 + \text{CO}$			$(1.64 \pm 0.16) \times 10^{-19}$		
	20 K $\text{CH}_4 + \text{CO}$			$(2.47 \pm 0.25) \times 10^{-19}$		
$\text{CO} + \text{H} \rightarrow \text{HCO}$ k_4 (in $\text{cm}^2 \text{s}^{-1}$)	5 K $\text{CH}_4 + \text{CO}$	$(1.27 \pm 0.13) \times 10^{-18}$	$(1.23 \pm 0.12) \times 10^{-18}$	$(4.07 \pm 0.41) \times 10^{-19}$	$(1.01 \pm 0.10) \times 10^{-18}$	$(3.57 \pm 0.36) \times 10^{-19}$
	5 K $\text{CD}_4 + \text{CO}$	$(6.07 \pm 0.61) \times 10^{-19}$	$(5.03 \pm 0.60) \times 10^{-19}$	$(3.01 \pm 0.30) \times 10^{-19}$	$(5.77 \pm 0.58) \times 10^{-19}$	$(2.01 \pm 0.20) \times 10^{-19}$
	10 K $\text{CH}_4 + \text{CO}$	$(1.43 \pm 0.14) \times 10^{-18}$	$(1.39 \pm 0.14) \times 10^{-18}$	$(6.63 \pm 0.67) \times 10^{-19}$	$(1.24 \pm 0.12) \times 10^{-18}$	$(6.59 \pm 0.66) \times 10^{-19}$
	15 K $\text{CH}_4 + \text{CO}$			$(1.49 \pm 0.15) \times 10^{-18}$		
	20 K $\text{CH}_4 + \text{CO}$			$(1.61 \pm 0.16) \times 10^{-18}$		
$\text{CH}_3 + \text{HCO} \rightarrow \text{CH}_3\text{CHO}$ k_5 (in $\text{cm}^2 \text{s}^{-1}$)	5 K $\text{CH}_4 + \text{CO}$	$(1.69 \pm 0.17) \times 10^{-18}$	$(9.09 \pm 0.91) \times 10^{-18}$	$(3.20 \pm 0.32) \times 10^{-19}$	$(6.09 \pm 0.61) \times 10^{-18}$	$(3.30 \pm 0.33) \times 10^{-19}$
	5 K $\text{CD}_4 + \text{CO}$	$(1.49 \pm 0.15) \times 10^{-18}$	$(8.49 \pm 0.85) \times 10^{-18}$	$(2.49 \pm 0.25) \times 10^{-19}$	$(3.29 \pm 0.33) \times 10^{-18}$	$(2.39 \pm 0.24) \times 10^{-19}$
	10 K $\text{CH}_4 + \text{CO}$	$(8.56 \pm 0.86) \times 10^{-19}$	$(2.76 \pm 0.28) \times 10^{-18}$	$(2.76 \pm 0.28) \times 10^{-19}$	$(3.15 \pm 0.32) \times 10^{-18}$	$(2.94 \pm 0.30) \times 10^{-19}$
	15 K $\text{CH}_4 + \text{CO}$			$(9.23 \pm 0.92) \times 10^{-19}$		
	20 K $\text{CH}_4 + \text{CO}$			$(1.81 \pm 0.19) \times 10^{-18}$		
$\text{HCO} + \text{H} \rightarrow \text{H}_2\text{CO}$ k_6 (in $\text{cm}^2 \text{s}^{-1}$)	5 K $\text{CH}_4 + \text{CO}$	$(2.10 \pm 0.21) \times 10^{-16}$	$(8.03 \pm 0.80) \times 10^{-16}$	$(7.09 \pm 0.71) \times 10^{-17}$	$(7.97 \pm 0.80) \times 10^{-16}$	$(6.50 \pm 0.65) \times 10^{-17}$
	5 K $\text{CD}_4 + \text{CO}$	$(1.81 \pm 0.18) \times 10^{-16}$	$(6.78 \pm 0.68) \times 10^{-16}$	$(6.08 \pm 0.61) \times 10^{-17}$	$(5.98 \pm 0.60) \times 10^{-16}$	$(5.51 \pm 0.55) \times 10^{-17}$
	10 K $\text{CH}_4 + \text{CO}$	$(1.60 \pm 0.16) \times 10^{-16}$	$(1.02 \pm 0.10) \times 10^{-15}$	$(6.51 \pm 0.65) \times 10^{-17}$	$(1.48 \pm 0.15) \times 10^{-15}$	$(6.46 \pm 0.65) \times 10^{-17}$
	15 K $\text{CH}_4 + \text{CO}$			$(3.45 \pm 0.35) \times 10^{-16}$		

Table 1
(Continued)

Reaction	Temperature	Rate Constant				
		Stage 1	Stage 2	Stage 3	Stage 4	Stage 5
	20 K CH ₄ + CO			$(5.13 \pm 0.51) \times 10^{-16}$		
C ₂ H ₆ → X k_X (in s ⁻¹)	5 K CH ₄ + CO	$(8.75 \pm 0.88) \times 10^{-5}$	$(8.76 \pm 0.88) \times 10^{-5}$	$(8.75 \pm 0.88) \times 10^{-5}$	$(8.73 \pm 0.88) \times 10^{-5}$	$(8.93 \pm 0.90) \times 10^{-5}$
	5 K CD ₄ + CO	$(9.89 \pm 1.00) \times 10^{-5}$	$(8.93 \pm 0.90) \times 10^{-5}$	$(8.95 \pm 0.90) \times 10^{-5}$	$(8.93 \pm 0.90) \times 10^{-5}$	$(8.96 \pm 0.90) \times 10^{-5}$
	10 K CH ₄ + CO	$(9.84 \pm 1.00) \times 10^{-5}$	$(9.80 \pm 1.00) \times 10^{-5}$	$(8.48 \pm 0.86) \times 10^{-5}$	$(9.83 \pm 1.00) \times 10^{-5}$	$(9.53 \pm 1.00) \times 10^{-5}$
	15 K CH ₄ + CO			$(1.19 \pm 0.12) \times 10^{-4}$		
	20 K CH ₄ + CO			$(1.62 \pm 0.17) \times 10^{-4}$		
CO → C + O $k_{CO_2 (1)}$ (in s ⁻¹)	5 K CH ₄ + CO	$(1.13 \pm 0.12) \times 10^{-4}$	$(1.05 \pm 0.11) \times 10^{-4}$	$(0.50 \pm 0.05) \times 10^{-4}$	$(0.42 \pm 0.04) \times 10^{-4}$	$(0.30 \pm 0.03) \times 10^{-4}$
	5 K CD ₄ + CO	$(1.23 \pm 0.13) \times 10^{-4}$	$(0.71 \pm 0.07) \times 10^{-4}$	$(0.70 \pm 0.07) \times 10^{-4}$	$(0.65 \pm 0.07) \times 10^{-4}$	$(0.60 \pm 0.06) \times 10^{-4}$
	10 K CH ₄ + CO	$(8.92 \pm 0.90) \times 10^{-5}$	$(8.87 \pm 0.89) \times 10^{-5}$	$(6.48 \pm 0.65) \times 10^{-5}$	$(4.64 \pm 0.47) \times 10^{-5}$	$(1.53 \pm 0.16) \times 10^{-5}$
	15 K CH ₄ + CO			$(4.85 \pm 0.50) \times 10^{-5}$		
	20 K CH ₄ + CO			$(6.17 \pm 0.62) \times 10^{-5}$		
CO + O → CO ₂ $k_{CO_2 (2)}$ (in cm ² s ⁻¹)	5 K CH ₄ + CO	$(5.35 \pm 0.54) \times 10^{-23}$	$(5.26 \pm 0.53) \times 10^{-23}$	$(2.55 \pm 0.26) \times 10^{-23}$	$(1.01 \pm 0.10) \times 10^{-23}$	$(1.05 \pm 0.10) \times 10^{-23}$
	5 K CD ₄ + CO	$(6.95 \pm 0.70) \times 10^{-23}$	$(6.75 \pm 0.68) \times 10^{-23}$	$(3.64 \pm 0.37) \times 10^{-23}$	$(2.03 \pm 0.21) \times 10^{-23}$	$(2.59 \pm 0.26) \times 10^{-23}$
	10 K CH ₄ + CO	$(9.11 \pm 0.92) \times 10^{-24}$	$(9.06 \pm 0.91) \times 10^{-24}$	$(6.36 \pm 0.65) \times 10^{-24}$	$(4.22 \pm 0.43) \times 10^{-24}$	$(1.13 \pm 0.12) \times 10^{-24}$
	15 K CH ₄ + CO			$(6.67 \pm 0.67) \times 10^{-24}$		
	20 K CH ₄ + CO			$(7.88 \pm 0.80) \times 10^{-24}$		
CO + CO → CO ₂ + C $k_{CO_2 (3)}$ (in cm ² s ⁻¹)	5 K CH ₄ + CO	$(1.42 \pm 0.15) \times 10^{-24}$	$(1.39 \pm 0.14) \times 10^{-24}$	$(1.02 \pm 0.11) \times 10^{-24}$	$(0.51 \pm 0.06) \times 10^{-24}$	$(0.50 \pm 0.05) \times 10^{-24}$
	5 K CD ₄ + CO	$(2.72 \pm 0.30) \times 10^{-24}$	$(2.43 \pm 0.25) \times 10^{-24}$	$(2.07 \pm 0.21) \times 10^{-24}$	$(1.95 \pm 0.20) \times 10^{-24}$	$(2.01 \pm 0.20) \times 10^{-24}$
	10 K CH ₄ + CO	$(5.23 \pm 0.53) \times 10^{-25}$	$(5.90 \pm 0.60) \times 10^{-25}$	$(4.64 \pm 0.47) \times 10^{-25}$	$(3.76 \pm 0.38) \times 10^{-25}$	$(1.23 \pm 0.13) \times 10^{-25}$
	15 K CH ₄ + CO			$(5.26 \pm 0.53) \times 10^{-25}$		
	20 K CH ₄ + CO			$(5.87 \pm 0.59) \times 10^{-25}$		

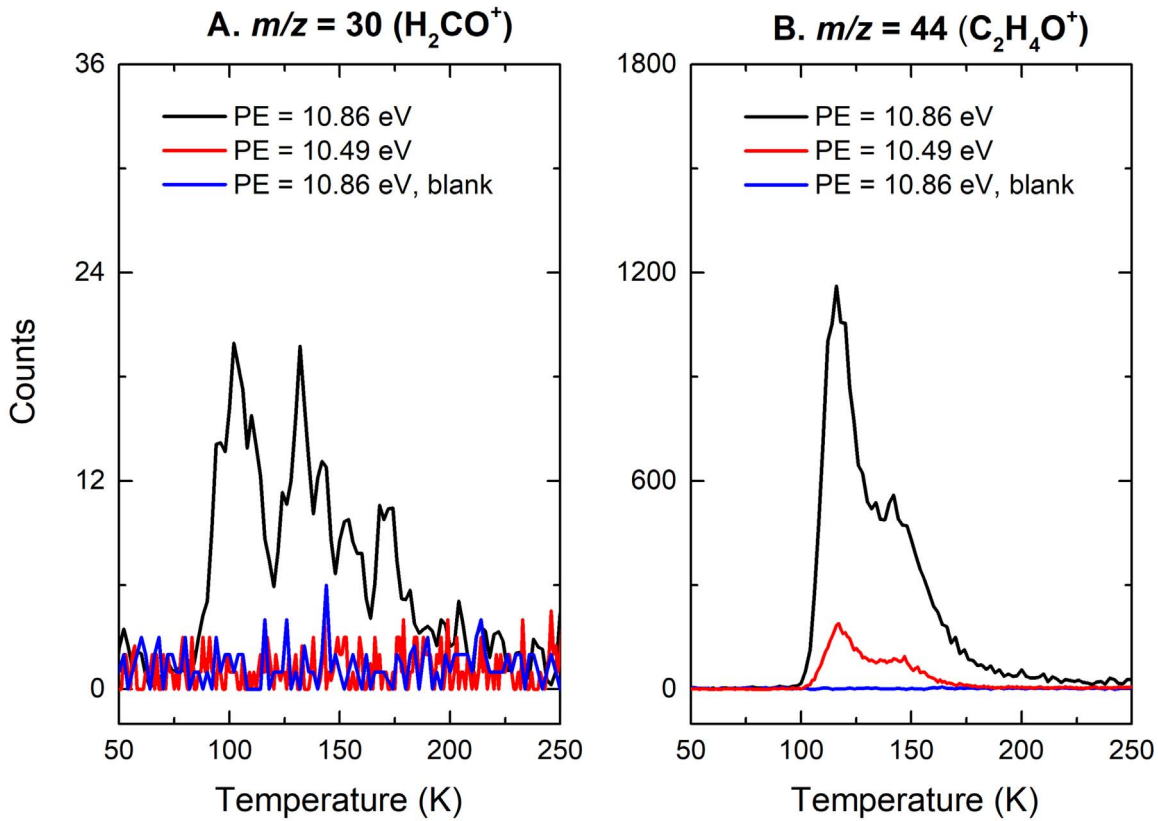


Figure 4. PI-ReTOF-MS data showing the temperature-programmed desorption profiles for (A) $m/z = 30$, H_2CO^+ , and (B) $m/z = 44$, $\text{C}_2\text{H}_4\text{O}^+$.

(IEs) of the species to selectively photoionize and detect their molecular ions at well-defined mass-to-charge ratios (m/z). Considering the experimentally determined IE of H_2CO (10.88 ± 0.01 eV) (Hernandez et al. 1977) along with the reduction in the IE of 0.03 eV by the Stark effect (Bergantini et al. 2018), photon energies of 10.86 eV ($\lambda = 114.166$ nm) and 10.49 eV ($\lambda = 118.222$ nm) were chosen. By comparing the TPD profiles for $m/z = 30$ (H_2CO^+) at PE = 10.86 and 10.49 eV, the sublimation event between 80 and 200 K can be assigned to H_2CO (Figure 4). The TPD profiles for $m/z = 44$ ($\text{C}_2\text{H}_4\text{O}^+$) at PE = 10.86 and 10.49 eV show a main peak at 116 K and a small shoulder at 142 K, which were previously confirmed to be CH_3CHO (IE = 10.23 ± 0.01 eV) and its vinyl alcohol isomer ($\text{H}_2\text{C}=\text{CHOH}$, IE = 9.17 ± 0.01 eV), respectively (Abplanalp et al. 2016). In blank experiments, which were performed under identical conditions but without irradiating the ices, no ion counts were detected, demonstrating that the identified signal is associated with the processing of the ices by energetic electrons.

4. Astrophysical Implications and Conclusions

To conclude, the present study provides the first compelling spectroscopic evidence of rapid radical-radical reactions involving formyl ($\text{HCO}\cdot$) and methyl ($\cdot\text{CH}_3$) along with atomic hydrogen and accompanying chemical desorption during the exposure of apolar interstellar model ices of methane (CH_4) and carbon monoxide (CO) to ionizing radiation with doses equivalent to those exposing the ice mantles in interstellar grains deep inside molecular clouds over 10^6 yr (Yeghikyan 2011; Abplanalp et al. 2016). These investigations reveal a strong temperature dependence of the ability of the ices to accumulate radicals. The overall concentrations of the

radicals can reach $(1.0 \pm 0.1)\%$ and $(1.1 \pm 0.1)\%$ (Table A10) prior to rapid radical-radical reactions at 5 K and 10 K, respectively. At 15 and 20 K, rapid radical-radical reactions were not observed, probably due to low radical ratios of $<0.8\%$. This temperature-related difference may affect the fundamental processes and reaction pathways leading to the formation of COMs, such as acetaldehyde, within interstellar analog ices at ultralow temperatures. These studies represent a very first step toward a systematic understanding of the critical role of rapid radical reactions in the formation of COMs in low-temperature interstellar ices and of how rapid radical-radical reactions may influence the injection of organics from icy grains (back) into the gas phase of molecular clouds like TMC-1. Pantaleone et al. (2020) revealed computationally a rapid dissipation of the reaction energy released in the formation of the formyl radical via addition of atomic hydrogen to carbon monoxide through thermal excitation of water molecules on interstellar grains within the first picosecond, the resulting formyl retaining insufficient energy to sublime into the gas phase from the icy grain. However, experimental studies observed measurable HCO desorption from the $\text{H} + \text{CO}$ reaction and H_2CO desorption during H-atom irradiation of H_2CO (Minissale et al. 2016a, 2016b).

The investigation of the fundamental processes and elementary mechanisms leading to an injection of complex organics from icy grains into the gas phase of cold molecular clouds at 10 K has just scratched the surface. Future studies are advised to systematically explore the effects of the ice composition (polar versus apolar, e.g., adding water) on the capability of interstellar (analog) ices to effectively store radicals. Whereas in molecular clouds, as a result of a fractionated condensation, nonpolar ices containing carbon monoxide and methane have

been suggested to deposit as “outer layers” onto water-rich (polar) ice material (Boogert et al. 2015), more homogeneous mixtures of polar (water, methanol) and nonpolar components (methane, carbon monoxide) have also been detected toward, e.g., VSSG 17 and IRS 51. Naturally, the chemical composition, in particular the potential presence of radical scavengers, is expected to influence the capability of interstellar ices to efficiently store radicals and to divert the reaction energy released from these exoergic radical–radical reactions (Pantaleone et al. 2020). Nevertheless, the rapid radical–radical reactions as presented here have the unique capability not only to synthesize new organic molecules within interstellar (model) ices at temperatures relevant to molecular clouds, but also to (re) distribute these organics from the grain into the gas phase via explosive desorption processes, once critical radical concentrations have accumulated within the icy grains. These injection processes may not be only relevant to the interstellar medium, but could also hold important implications for the solar system and for rapid outbursts of comets such as 29P/Schwassmann–Wachmann 1 (Gronkowski & Wesołowski 2016) and Comet 17P/Holmes (Ishiguro et al. 2013), as cometary ices may also accumulate radicals—at the low temperatures of Oort’s cloud—formed by GCRs to levels that are able to trigger explosive reactions—a plausible alternative to not-yet-proven scenarios involving thermal stress in the nucleus (Gronkowski 2007), the phase change of water, the polymerization of hydrogen cyanide (Gronkowski & Sacharczuk 2010), or sudden sublimation of carbon monoxide.

This work was supported by the US National Science Foundation (Astronomy) under Grant NSF-AST 1800975. We would also like to acknowledge the W.M. Keck Foundation for funding the construction of the surface science machine.

Appendix

A.1. Simulation Experiments

The experiments were carried out at the W. M. Keck Research Laboratory in Astrochemistry (Jones & Kaiser 2013), which has been used to simulate the formation of complex organic molecules detected in the interstellar medium (Table A1). The experimental setup includes a contamination-free ultrahigh-vacuum chamber pumped to a few 10^{-11} Torr by two magnetically suspended turbomolecular pumps backed by an oil-free scroll pump. A polished silver substrate was mounted to a cold head capable of achieving 5.0 K by a two-stage closed-cycle helium refrigerator (Sumitomo Heavy Industries, RDK-415E). The temperature of the silver target was monitored and regulated by a high-precision silicon diode and a programmable temperature controller, respectively. After the wafer reached specific temperatures (5, 10, 15, and 20 K), methane (CH_4 , Specialty Gases of America, 99.999%) or ethane (C_2H_6 , Gaspro, 99.999%) and carbon monoxide (CO, Aldrich, 99.99%; C^{18}O , Aldrich, 99% ^{18}O) (Tables A2–A7) were premixed in a gas mixing chamber and deposited on the substrate through a glass capillary array to form ice mixtures of CH_4/CO , CD_4/CO , and $\text{C}_2\text{H}_6/\text{C}^{18}\text{O}$. Ice thicknesses were determined using laser interferometry by measuring the interference patterns using an He–Ne 632.8 nm laser (Hollenberg & Dows 1961; Turner et al. 2015). Considering the incidence angle of the laser (2°) and the refractive indices of CH_4 ($n_{\text{CH}_4} = 1.34 \pm 0.04$) (Satorre et al. 2008; Bouilloud et al. 2015), C_2H_6 ($n_{\text{C}_2\text{H}_6} = 1.28 \pm 0.03$) (Satorre et al. 2017), and CO ($n_{\text{CO}} = 1.25 \pm 0.03$) (Bouilloud et al. 2015; Turner et al. 2015), the ice thicknesses were calculated

to be up to 1050 ± 100 nm. After the deposition, an FTIR spectrometer (Nicolet 6700), operating in absorption–reflection–absorption mode, was utilized to probe the chemical modifications of the ices in situ in the range $6000\text{--}600\text{ cm}^{-1}$ with 4 cm^{-1} spectral resolution (Figures 1–3, A1, and A2). Detailed assignments of the FTIR spectra were compiled in Tables A5–A7 (Pacansky & Dupuis 1982; Socrates 2004; Hudson et al. 2014; Bouilloud et al. 2015). Exploiting a modified Beer–Lambert law (Hollenberg & Dows 1961; Turner et al. 2015) and the absorption coefficients (A value) of CH_4 ($3.5 \times 10^{-19}\text{ cm molecule}^{-1}$ for 4205 cm^{-1} ($\nu_1 + \nu_4$) and $5.3 \times 10^{-19}\text{ cm molecule}^{-1}$ for 4301 cm^{-1} ($\nu_3 + \nu_4$)) (Brunetto et al. 2008; Bouilloud et al. 2015), CO ($1.04 \times 10^{-19}\text{ cm molecule}^{-1}$ for 4253 cm^{-1} ($2\nu_1$)) (Gerakines et al. 2005; Bouilloud et al. 2015), and C_2H_6 ($2.18 \times 10^{-19}\text{ cm molecule}^{-1}$ for 4325 cm^{-1} (ν_{10})) (Hudson et al. 2014), the ice compositions were determined as compiled in Table A2. The ices were then irradiated at well-defined temperatures with 5 keV electrons (Table A3). Utilizing Monte Carlo simulations (CASINO 2.42) (Drouin et al. 2007), the average depths of the 5 keV electrons were calculated to be 440 ± 40 nm for CH_4/CO ices and 360 ± 40 nm for $\text{C}_2\text{H}_6/\text{C}^{18}\text{O}$ ices (Table A3), which are less than the thicknesses of the ices, thus ensuring no interaction between the electrons and the silver substrate. The irradiation doses (Table A3) correspond to those received by ice mantles inside molecular clouds during their typical lifetime of 10^6 yr (Yeghikyan 2011; Abplanalp et al. 2016). The doses are presented in eV amu^{-1} , which can be converted to eV per molecule by multiplying the value by the atomic mass of the corresponding molecule (e.g., 28 amu for CO). During the irradiation, the samples were continuously monitored by the FTIR spectrometer at intervals of 1 or 2 minutes. The molecules in the gas phase were monitored using an Extrel 5221 QMS with an electron impact energy of 70 eV.

After the irradiation, the ices were heated to 300 K at a rate of 1 K min^{-1} (TPD). During the TPD phase, any subliming molecules were detected using a ReTOF mass spectrometer (Jordan TOF Products, Inc.) with single photon ionization (Jones & Kaiser 2013) (Figure 4). This photoionization process utilizes difference four-wave mixing to produce vacuum ultraviolet light ($\omega_{\text{vuv}} = 2\omega_1 - \omega_2$) (Table A4). The experiments were performed with a photoionization energy of 10.86 eV and repeated at 10.49 eV to confirm H_2CO . To produce 10.86 eV, the second harmonic (532 nm) of an Nd:YAG laser was used to pump a Rhodamine 610/640 dye mixture ($0.17/0.04\text{ g l}^{-1}$ ethanol) to obtain 606.948 nm (2.04 eV) (Sirah, Cobra-Stretch), which underwent a frequency tripling process to achieve $\omega_1 = 202.316$ nm (6.13 eV) ($\beta\text{-BaB}_2\text{O}_4$ crystals, 44° and 77°). A second Nd:YAG laser (second harmonic at 532 nm) pumped an LDS 867 dye (0.15 g l^{-1} ethanol) to obtain $\omega_2 = 888$ nm (1.40 eV), which then combined with $2\omega_1$, using krypton as a nonlinear medium, and generated $\omega_{\text{vuv}} = 114.166$ nm (10.86 eV) at 10^{12} photons per pulse. The 10.49 eV (118.222 nm) light was generated via frequency tripling ($\omega_{\text{vuv}} = 3\omega_1$) of the third harmonic (355 nm) of the fundamental of an Nd:YAG laser (YAG A) in pulsed gas jets of Xe. The VUV light was separated from other wavelengths (due to multiple resonant and nonresonant processes (e.g., $2\omega_1 + \omega_2$) using a lithium fluoride (LiF) biconvex lens (ISP Optics) and directed 2 mm above the sample to ionize the sublimed molecules. The ionized molecules were mass-analyzed with the ReTOF mass spectrometer where the arrival time at a multichannel plate is based on mass-to-charge ratios, and the signal was amplified with a fast preamplifier (Ortec 9305) and recorded

Table A1
Complex Organic Molecules (COMs) Detected in TMC-1

Species	Gas-phase Formation Pathways	References
Formaldehyde (H ₂ CO)	$\text{CH}_3^+ + \text{O} \rightarrow \text{CH}_2\text{O}^+ + \text{H}$ $\text{CH}_2\text{O}^+ + \text{H}_2 \rightarrow \text{CH}_2\text{OH}^+ + \text{H}$ $\text{CH}_2\text{OH}^+ + e^- \rightarrow \text{H}_2\text{CO}$	Soma et al. (2018)
Methanol (CH ₃ OH)	$\text{CH}_3^+ + \text{H}_2\text{O} \rightarrow \text{CH}_3\text{OH}_2^+ + h\nu$ $\text{CH}_3\text{OH}_2^+ + e^- \rightarrow \text{CH}_3\text{OH} + \text{H}$	Pratap et al. (1997), Garrod et al. (2006), Herbst (1991), Geppert et al. (2006)
Formic acid (HCOOH)	$\text{HCO}^+ + \text{H}_2\text{O} \rightarrow \text{HCOOH}_2^+ + h\nu$ $\text{CH}_4 + \text{O}_2^+ \rightarrow \text{HCOOH}_2^+ + \text{H}$ $\text{HCOOH}_2^+ + e^- \rightarrow \text{HCOOH} + \text{H}$	Smith et al. (2004), Irvine et al. (1990), Leung et al. (1984)
Acetaldehyde (CH ₃ CHO)	$\text{CH}_3^+ + \text{H}_2\text{CO} \rightarrow \text{CH}_3\text{CHOH}^+ + h\nu$ $\text{CH}_3\text{CHOH}^+ + e^- \rightarrow \text{CH}_3\text{CHO} + \text{H}$ $\text{C}_2\text{H}_5 + \text{O} \rightarrow \text{CH}_3\text{CHO} + \text{H}$	Mathews et al. (1985), Huntress & Mitchell (1979) Vasyunin & Herbst (2013)
Methyl formate (HCOOCH ₃)	$\text{H}_2\text{COH}^+ + \text{H}_2\text{CO} \rightarrow \text{H}_2\text{CO} \cdots \text{H} \cdots \text{OCH}_2^+ + h\nu$ $\text{H}_2\text{CO} \cdots \text{H} \cdots \text{OCH}_2^+ + e^- \rightarrow \text{HCOOCH}_3 + \text{H}$ $\text{CH}_3^+ + \text{HCOOH} \rightarrow \text{HC(OH)OCH}_3^+ + h\nu$ $\text{HC(OH)OCH}_3^+ + e^- \rightarrow \text{HCOOCH}_3 + \text{H}$ $\text{CH}_3\text{OH} + \text{OH} \rightarrow \text{CH}_3\text{O} + \text{H}_2\text{O}$ $\text{CH}_3\text{O} + \text{CH}_3 \rightarrow \text{CH}_3\text{OCH}_3 + h\nu$ $\text{CH}_3\text{OCH}_3 + \text{F} \rightarrow \text{CH}_3\text{OCH}_2 + \text{HF}$ $\text{CH}_3\text{OCH}_2 + \text{O} \rightarrow \text{HCOOCH}_3 + \text{H}$	Soma et al. (2018), Vasyunin & Herbst (2013) Balucani et al. (2015)
Ketene (H ₂ C=C=O)	$\text{CH}_3^+ + \text{CO} \rightarrow \text{CH}_3\text{CO}^+ + h\nu$ $\text{CH}_3\text{CO}^+ + e^- \rightarrow \text{H}_2\text{C}=\text{C}=\text{O} + \text{H}$	Soma et al. (2018), Ruiterkamp et al. (2007), Turner et al. (1999)
Cyclopropenone (c-C ₃ H ₂ O)	$c\text{-C}_3\text{H}_4^+ + \text{O} \rightarrow c\text{-C}_3\text{H}_3\text{O}^+ + \text{H}$ $c\text{-C}_3\text{H}_3\text{O}^+ + e^- \rightarrow c\text{-C}_3\text{H}_2\text{O} + \text{H}$ $c\text{-C}_3\text{H}_2 + \text{O} \rightarrow c\text{-C}_3\text{H}_2\text{O}$ $c\text{-C}_3\text{H}_2 + \text{O}_2 \rightarrow c\text{-C}_3\text{H}_2\text{O} + \text{O}$	Soma et al. (2018), Quan & Herbst (2007) Ahmadvand et al. (2014), Hollis et al. (2006)
Dimethyl ether (CH ₃ OCH ₃)	$\text{CH}_3^+ + \text{CH}_3\text{OH} \rightarrow \text{CH}_3\text{OCH}_4^+ + h\nu$ $\text{CH}_3\text{OCH}_4^+ + e^- \rightarrow \text{CH}_3\text{OCH}_3 + \text{H}$ $\text{CH}_3\text{OH} + \text{OH} \rightarrow \text{CH}_3\text{O} + \text{H}_2\text{O}$ $\text{CH}_3\text{O} + \text{CH}_3 \rightarrow \text{CH}_3\text{OCH}_3 + h\nu$	Soma et al. (2018), Vasyunina et al. (2013) Balucani et al. (2015)
Propynal (HC ≡ CCHO)	$\text{C}_2\text{H}_3^+ + \text{CO} \rightarrow \text{H}_3\text{C}_3\text{O}^+ + h\nu$ $\text{H}_3\text{C}_3\text{O}^+ + e^- \rightarrow \text{HC} \equiv \text{C} - \text{CHO} + \text{H}$ $\text{C}_2\text{H} + \text{H}_2\text{CO} \rightarrow \text{HC} \equiv \text{C} - \text{CHO} + \text{H}$	Irvine et al. (1988) Petrie (1995)

Table A2
List of Experiments

	Irradiation Temperature (K)	Irradiation Current and Time	Precursors
1	5	30 nA, 13 minutes	CH ₄ + CO ((1.3 ± 0.2) : 1)
2	5	30 nA, 60 minutes	CH ₄ + CO ((1.3 ± 0.2) : 1)
3	5	30 nA, 60 minutes	CD ₄ + CO ((1.2 ± 0.2) : 1)
4	5	30 nA, 60 minutes	C ₂ H ₆ + C ¹⁸ O ((1.5 ± 0.3) : 1)
5	10	30 nA, 60 minutes	CH ₄ + CO ((1.1 ± 0.2) : 1)
6	15	30 nA, 60 minutes	CH ₄ + CO ((1.2 ± 0.2) : 1)
7	20	30 nA, 60 minutes	CH ₄ + CO ((1.1 ± 0.2) : 1)

with a multichannel scalar (MCS, FAST ComTec, P7888-1 E), which is triggered by a pulse generator at 30 Hz. Each ReTOF spectrum is the average of 3600 sweeps of the mass spectrum in 4 ns bin widths, which correspond to an increase in the sample temperature of 2 K.

A.2. Optical Interference Effects

Teolis et al. demonstrated that for absorption–reflection–absorption FTIR spectroscopy, the absorbance of strong bands is not guaranteed to be linear with respect to ice thickness due

Table A3

Data Applied to Calculate the Average Irradiation Dose per Molecule

Initial kinetic energy of the electrons, E_{init} (keV)	5	5
Ice	CH ₄ + CO	C ₂ H ₆ + C ¹⁸ O
Irradiation current, I (nA)	30 ± 2	30 ± 2
Total number of electrons	(6.7 ± 0.3) × 10 ¹⁴	(6.7 ± 0.3) × 10 ¹⁴
Average penetration depth, l_{ave} (nm) ^a	440 ± 40	360 ± 40
Average kinetic energy of back-scattered electrons, E_{bs} (keV) ^a	3.26 ± 0.33	3.24 ± 0.32
Fraction of backscattered electrons, f_{bs} ^a	0.34 ± 0.03	0.33 ± 0.03
Average kinetic energy of transmitted electrons, E_{trans} (keV) ^a	0	0
Fraction of transmitted electrons, f_{trans} ^a	0	0
Irradiated area, A (cm ²)	1.0 ± 0.1	1.0 ± 0.1
Dose (eV amu ⁻¹)	0.160 ± 0.025	0.201 ± 0.032

Note.^a Parameters obtained from CASINO software v2.42.**Table A4**Parameters for the Vacuum Ultraviolet Light Generation Used in the Present Experiments^a

$2\omega_1 - \omega_2$	Photoionization energy (eV)	10.86	10.49 (3 ω_1)
	Flux (10 ¹¹ photons s ⁻¹)	10 ± 1	12 ± 1
	Wavelength (nm)	114.166	118.222
ω_1	Wavelength (nm)	202.316	355
Nd:YAG (YAG A)	Wavelength (nm)	532	355
Dye laser (DYE A)	Wavelength (nm)	606.948	...
Dye	Rhodamine 610 and 640
ω_2	Wavelength (nm)	888	...
Nd:YAG (YAG B)	Wavelength (nm)	532	...
Dye laser (DYE B)	Wavelength (nm)	888	...
Dye	LDS 867
	Nonlinear medium	Kr	Xe

Note.^a The uncertainty for VUV photon energies is 0.01 eV.

to optical interference effects (Teolis et al. 2007). However, this issue can be circumvented by selecting weak peaks because their band strengths still have a linear relationship with the amount of ice deposited (Öberg et al. 2009a; Maksyutenko et al. 2015). Therefore, the column densities of each species were determined based on integrated areas of their weak peaks and corresponding absorption coefficients exploiting a modified Beer–Lambert law (Hollenberg & Dows 1961; Turner et al. 2015).

Table A5Infrared Absorption Peaks Recorded before and after Irradiation of Methane (CH₄) + Carbon Monoxide (CO) Ice^a

Before Irradiation (cm ⁻¹)	After Irradiation (cm ⁻¹)	Assignment
4534, 4301, 4205		$\nu_2 + \nu_3, \nu_3 + \nu_4, \nu_1 + \nu_4$ (CH ₄)
4253		2 ν_1 (CO)
	3255	ν_3 (C ₂ H ₂)
	3153	ν_3 (CH ₃)
	3092	ν_9 (C ₂ H ₄)
3012		ν_3 (CH ₄)
	2979	ν_{10} (C ₂ H ₆)
	2961	ν_1 (C ₂ H ₆)
	2943	$\nu_8 + \nu_{11}$ (C ₂ H ₆)
	2922	$\nu_8 + \nu_{11}$ (C ₂ H ₆)
2907		ν_1 (CH ₄)
	2886	ν_5 (C ₂ H ₆)
2819		$\nu_2 + \nu_4$ (CH ₄)
	2746	$\nu_2 + \nu_6$ (C ₂ H ₆)
2596		2 ν_4 (CH ₄)
	2341	ν_3 (CO ₂)
	2277	ν_3 (¹³ CO ₂)
2136		ν_1 (CO)
2092		ν_1 (¹³ CO)
	1853	ν_3 (HCO)
	1750–1680	ν (C=O)
	1465	ν_{11} (C ₂ H ₆)
	1428	ν_{12} (CH ₃ CHO)
	1375	ν_6 (C ₂ H ₆)
	1351	ν_7 (CH ₃ CHO)
1303		ν_4 (CH ₄)
	1123	ν_8 (CH ₃ CHO)
	1093	ν_2 (HCO)
	956	ν_7 (C ₂ H ₄)
	822	ν_{12} (C ₂ H ₆)

Note.^a References: Socrates (2004), Abplanalp et al. (2016).**A.3. Reaction Scheme**

In the reaction scheme (Table A8), radiolysis of C₂H₆ to higher-order hydrocarbons (X) was streamlined to one reaction (Reaction X). To account for the formation of carbon dioxide, three reactions, i.e., energetic electron-induced dissociation of carbon monoxide to carbon and oxygen atoms (Reaction CO₂(1)), recombination of CO and O to CO₂ (Reaction CO₂(2)), and

Table A6Infrared Absorption Peaks Recorded before and after Irradiation of Deuterated Methane (CD₄) + Carbon Monoxide (CO) Ice^a

Before Irradiation (cm ⁻¹)	After Irradiation (cm ⁻¹)	Assignment
3241, 3090		$\nu_3 + \nu_4, \nu_1 + \nu_4$ (CD ₄)
4250		$2\nu_1$ (CO)
	2446	ν_3 (C ₂ D ₂)
	2373	ν_3 (CD ₃)
2253		ν_3 (CD ₄)
	2232	ν_{10} (C ₂ D ₆)
	2215	ν_1 (C ₂ D ₆)
	2095	$\nu_8 + \nu_{11}$ (C ₂ D ₆)
2098		ν_1 (CD ₄)
	2082	ν_5 (C ₂ D ₆)
	1946	$\nu_2 + \nu_6$ (C ₂ D ₆)
1979		$2\nu_4$ (CD ₄)
	2341	ν_3 (CO ₂)
	2277	ν_3 (¹³ CO ₂)
2136		ν_1 (CO)
2092		ν_1 (¹³ CO)
	1795	ν_3 (DCO)
	1725–1660	ν (C=O)
	1025	ν_{12} (CD ₃ CDO)
	1157	ν_7 (CD ₃ CDO)
992		ν_4 (CD ₄)

Note.^a References. Socrates (2004), Kaiser et al. (2014).

reaction of electronically excited carbon monoxide (CO*) with neighboring ground-state CO producing CO₂ and C (Reaction CO₂(3)), were added to the reaction scheme (Table A8).

A.4. Radical Concentration

The column densities of electron irradiation-induced methyl radical (\bullet CH₃), ethane (C₂H₆), carbon dioxide (CO₂), formyl radical (HCO \bullet), formaldehyde (H₂CO), and acetaldehyde (CH₃CHO) were calculated based on the absorptions at 3153 cm⁻¹ ($A = 2.5 \times 10^{-18}$ cm molecule⁻¹) (Snelson 1970; Wormhoudt & McCurdy 1989; Bennett et al. 2005a), 2979 cm⁻¹ ($A = 2.1 \times 10^{-17}$ cm molecule⁻¹) (Hudson et al. 2014), 2341 cm⁻¹ ($A = 1.1 \times 10^{-16}$ cm molecule⁻¹) (Bouilloud et al. 2015), 1853 cm⁻¹ ($A = 1.5 \times 10^{-17}$ cm molecule⁻¹) (Hudson & Moore 1999; Bennett et al. 2005a), 1725 cm⁻¹ ($A = 1.6 \times 10^{-17}$ cm molecule⁻¹), contribution of CH₃CHO was excluded) (Bouilloud et al. 2015), and 1351 cm⁻¹ ($A = 4.5 \times 10^{-18}$ cm molecule⁻¹) (Bennett et al. 2005b), respectively (Tables A9 and A10). No absorptions of methylene (CH₂) were observed. Considering that its strongest peak (ν_2 bending mode, $A = 2.0 \times 10^{-18}$ cm molecule⁻¹) (Bennett et al. 2006) is comparable

Table A7Infrared Absorption Peaks Recorded before and after Irradiation of Ethane (C₂H₆) + ¹⁸O-carbon Monoxide (C¹⁸O) Ice^a

Before Irradiation (cm ⁻¹)	After Irradiation (cm ⁻¹)	Assignment
4401, 4353, 4325, 4272, 4252, 4187, 4159, 4126, 4086, 4069		$\nu_8 + \nu_{10}, \nu_2 + \nu_7, \nu_6 + \nu_{10}, \nu_1 + \nu_6, \nu_2 + \nu_5, \nu_7 + \nu_{12}, \nu_7 + \nu_{12}, \nu_8 + \nu_{11} + \nu_{12}, \nu_8 + \nu_{11} + \nu_{12}, \nu_5 + \nu_{12}$ (C ₂ H ₆)
4146		$2\nu_1$ (C ¹⁸ O)
3259		$\nu_4 + \nu_7$ (C ₂ H ₆)
	3106	ν_{10} (C ₂ H ₅)
	3090	ν_9 (C ₂ H ₄)
	3009	ν_3 (CH ₄)
2975		ν_{10} (C ₂ H ₆)
2956		ν_1 (C ₂ H ₆)
2943		$\nu_8 + \nu_{11}$ (C ₂ H ₆)
2915		$\nu_8 + \nu_{11}$ (C ₂ H ₆)
2882		ν_5 (C ₂ H ₆)
2853		$\nu_2 + \nu_4 + \nu_{12}$ (C ₂ H ₆)
2826		$\nu_6 + \nu_{11}$ (C ₂ H ₆)
2737		$\nu_2 + \nu_6$ (C ₂ H ₆)
2649		$\nu_8 + \nu_{12}$ (C ₂ H ₆)
2557		$\nu_6 + \nu_9$ (C ₂ H ₆)
2358		$\nu_3 + \nu_6$ (C ₂ H ₆)
	2335	ν_3 (¹⁸ OCO)
	2321	ν_3 (CO ₂)
	2312	ν_3 (C ¹⁸ O ₂)
2136		ν_1 (CO)
2089		ν_1 (C ¹⁸ O)
	1812	ν_3 (HC ¹⁸ O)
	1720–1650	ν (C= ¹⁸ O)
1462		ν_{11} (C ₂ H ₆)
	1436	ν_{12} (C ₂ H ₄)/ ν_8 (C ₂ H ₅ O ¹⁸ H)
1370		ν_6 (C ₂ H ₆)
	1300	ν_4 (CH ₄)
	951	ν_7 (C ₂ H ₄)
820		ν_{12} (C ₂ H ₆)

Note.^a References. Socrates (2004), Abplanalp et al. (2016).

with the 3153 cm⁻¹ peak of CH₃ ($A = 2.5 \times 10^{-18}$ cm molecule⁻¹), even though CH₂ is formed in the present experiments, the amount probably is well below that of CH₃. Previous studies found that the CH₂ formed during 9 MeV α -particle ion irradiation of CH₄ ice is about three orders of magnitude less than the CH₃ (Kaiser et al. 1997).

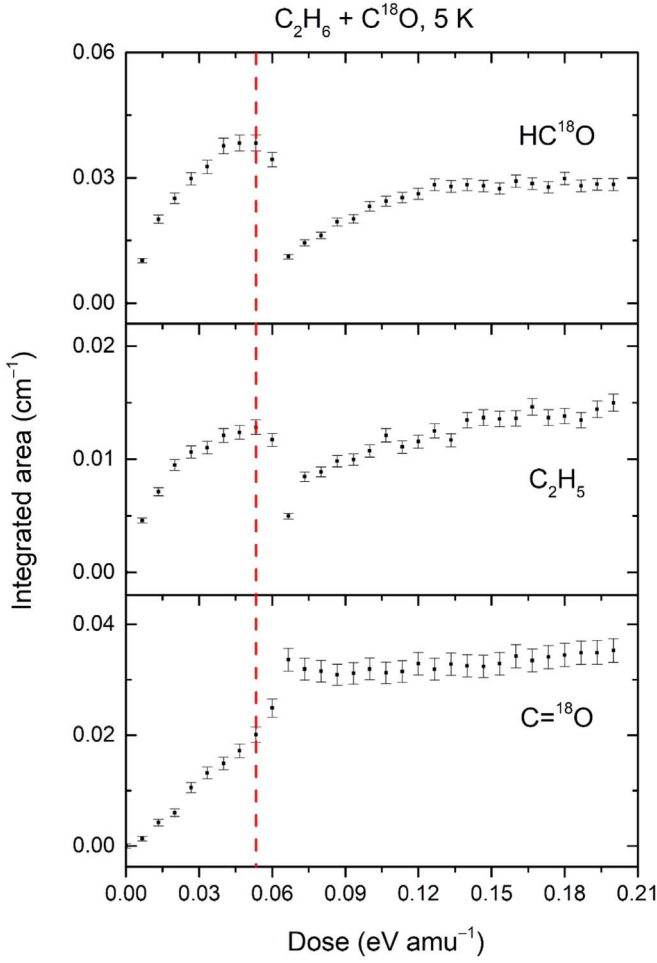


Figure A1. Temporal profiles of the integrated areas (cm^{-1}) of ^{18}O -formyl radical (HC^{18}O), ethyl radical (C_2H_5), and ^{18}O -carbonyl group (C^{18}O) during the irradiation of ethane (C_2H_6) + ^{18}O -carbon monoxide (C^{18}O) ice.

Monte Carlo simulations (CASINO 2.42) (Drouin et al. 2007) found that 90% of the energy of impinging electrons is absorbed by the molecules in the 200 nm top layer of methane + carbon monoxide ice. Therefore, the majorities of the above mentioned products reside in this region.

A.5. Contribution of Rapid Radical Reactions

In stages 2 and 4 of the 5 and 10 K experiments, the sudden increases in the column densities of C_2H_6 , H_2CO , and CH_3CHO can be separated into parts: regular rises and rapid radical reaction-induced rises. The contributions of rapid radical reactions were calculated from the column densities

Table A8
Reaction Rate Equations^a

Reaction	Rate Equation
$\text{CH}_4 \rightarrow \text{CH}_3 + \text{H}$ k_1 (in s^{-1})	$r_1 = k_1 \times [\text{CH}_4]$
$\text{CH}_4 + \text{CH}_4 \rightarrow \text{C}_2\text{H}_6 + 2\text{H}$ k_2 (in $\text{cm}^2 \text{s}^{-1}$)	$r_2 = k_2 \times [\text{CH}_4] \times [\text{CH}_4]$
$\text{CH}_3 + \text{CH}_3 \rightarrow \text{C}_2\text{H}_6$ k_3 (in $\text{cm}^2 \text{s}^{-1}$)	$r_3 = k_3 \times [\text{CH}_3] \times [\text{CH}_3]$
$\text{CO} + \text{H} \rightarrow \text{HCO}$ k_4 (in $\text{cm}^2 \text{s}^{-1}$)	$r_4 = k_4 \times [\text{CO}] \times [\text{H}]$
$\text{CH}_3 + \text{HCO} \rightarrow \text{CH}_3\text{CHO}$ k_5 (in $\text{cm}^2 \text{s}^{-1}$)	$r_5 = k_5 \times [\text{CH}_3] \times [\text{HCO}]$
$\text{HCO} + \text{H} \rightarrow \text{H}_2\text{CO}$ k_6 (in $\text{cm}^2 \text{s}^{-1}$)	$r_6 = k_6 \times [\text{HCO}] \times [\text{H}]$
$\text{C}_2\text{H}_6 \rightarrow \text{X}$ k_X (in s^{-1})	$r_X = k_X \times [\text{C}_2\text{H}_6]$
$\text{CO} \rightarrow \text{C} + \text{O}$ $k_{\text{CO}_2(1)}$ (in s^{-1})	$r_{\text{CO}_2(1)} = k_{\text{CO}_2(1)} \times [\text{CO}]$
$\text{CO} + \text{O} \rightarrow \text{CO}_2$ $k_{\text{CO}_2(2)}$ (in $\text{cm}^2 \text{s}^{-1}$)	$r_{\text{CO}_2(2)} = k_{\text{CO}_2(2)} \times [\text{CO}] [\text{O}]$
$\text{CO} + \text{CO} \rightarrow \text{CO}_2 + \text{C}$ $k_{\text{CO}_2(3)}$ (in $\text{cm}^2 \text{s}^{-1}$)	$r_{\text{CO}_2(3)} = k_{\text{CO}_2(3)} \times [\text{CO}] \times [\text{CO}]$
$\frac{d[\text{CH}_4]}{dt} = -r_1 - r_2 - r_3$ $\frac{d[\text{CH}_3]}{dt} = r_1 - r_3 - r_3 - r_5$ $\frac{d[\text{H}]}{dt} = r_1 + r_2 + r_3 - r_4 - r_6$ $\frac{d[\text{C}_2\text{H}_6]}{dt} = r_2 + r_3 - r_X$ $\frac{d[\text{CO}]}{dt} = -r_4 - r_{\text{CO}_2(1)} - r_{\text{CO}_2(2)} - r_{\text{CO}_2(3)} - r_{\text{CO}_2(3)}$ $\frac{d[\text{HCO}]}{dt} = r_4 - r_5 - r_6$ $\frac{d[\text{CH}_3\text{CHO}]}{dt} = r_5$ $\frac{d[\text{H}_2\text{CO}]}{dt} = r_6$ $\frac{d[\text{X}]}{dt} = r_X$ $\frac{d[\text{C}]}{dt} = r_{\text{CO}_2(1)} - r_{\text{CO}_2(3)}$ $\frac{d[\text{O}]}{dt} = r_{\text{CO}_2(1)} - r_{\text{CO}_2(2)}$ $\frac{d[\text{CO}_2]}{dt} = r_{\text{CO}_2(2)} + r_{\text{CO}_2(3)}$	

Note.

^a r_1 , k_1 , $[\text{CH}_4]$ represent reaction rate of reaction 1, rate constant of reaction 1, and column density of CH_4 , respectively.

of these species at the end of these stages minus contributions of regular rises, which were simulated using the data in previous stages (e.g., using the rate constants in stage 1 to simulate the column densities of these species at the end of stage 2). Table A11 compiles the contribution ratios of rapid radical reactions and confirms that these processes play critical roles in the formation of C_2H_6 , H_2CO , and CH_3CHO .

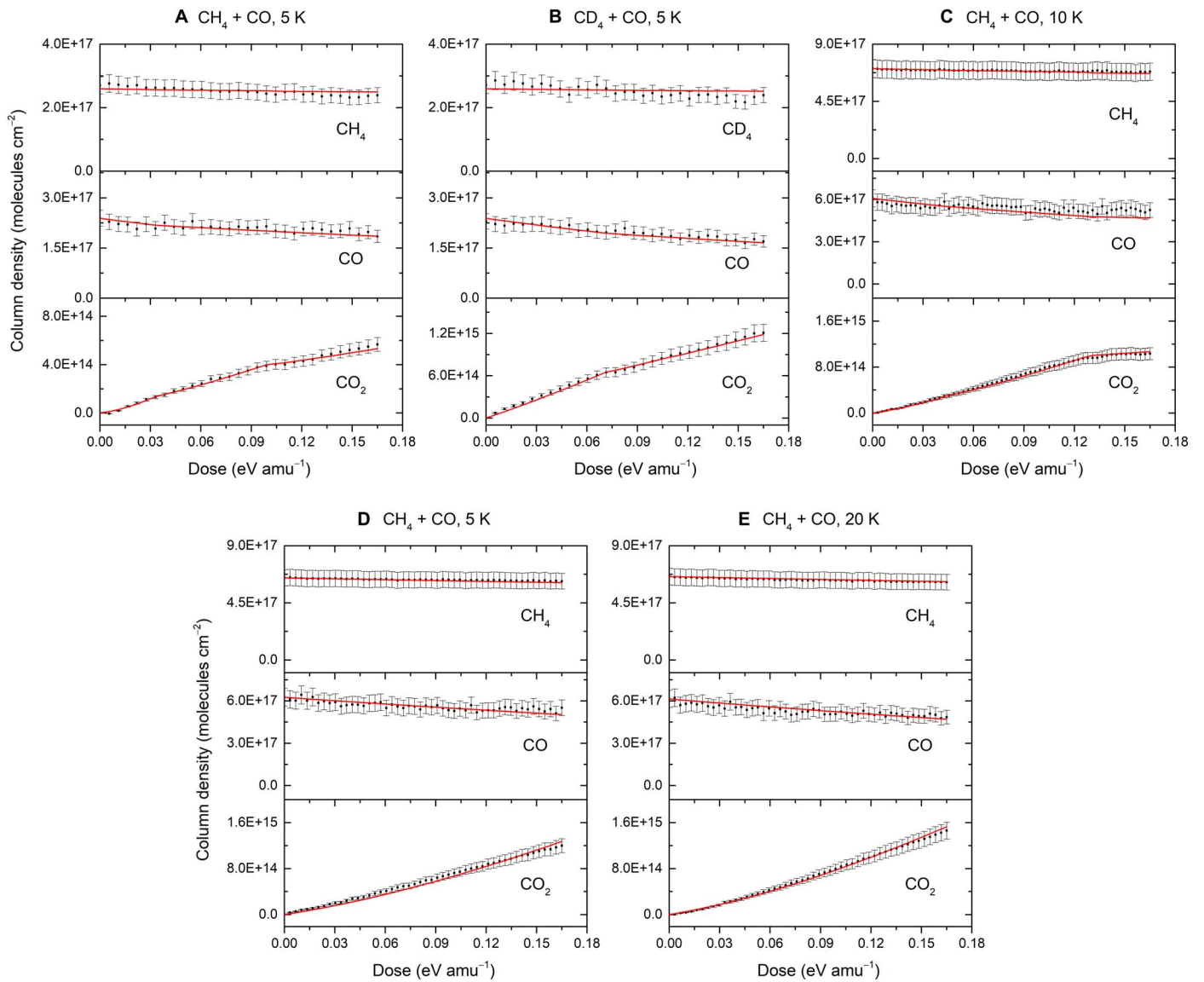


Figure A2. Temporal profiles of the column densities of methane (CH₄), carbon monoxide (CO), and carbon dioxide (CO₂) during the irradiation (30 nA, 60 minutes). The kinetic fits (red lines) are shown for each species, accounting for the reaction scheme as compiled in Table A8.

Table A9
Mass Balance of Methyl (CH₃) and Formyl Radicals (HCO) (in molecules cm⁻²)

Systems		CH ₃		HCO	
		Formation CH ₄ → CH ₃ + H	Consumption CH ₃ + 2 × C ₂ H ₆ + CH ₃ CHO	Formation CO + H → HCO	Consumption HCO + CH ₃ CHO + H ₂ CO
5 K CH ₄ + CO	Stage 1	$(1.91 \pm 0.20) \times 10^{15}$	$(1.87 \pm 0.19) \times 10^{15}$	$(1.69 \pm 0.17) \times 10^{15}$	$(1.61 \pm 0.16) \times 10^{15}$
	Stage 2	$(2.76 \pm 0.28) \times 10^{15}$	$(2.70 \pm 0.27) \times 10^{15}$	$(2.11 \pm 0.20) \times 10^{15}$	$(2.03 \pm 0.20) \times 10^{15}$
	Stage 3	$(6.26 \pm 0.63) \times 10^{15}$	$(5.75 \pm 0.58) \times 10^{15}$	$(4.81 \pm 0.50) \times 10^{15}$	$(4.62 \pm 0.47) \times 10^{15}$
	Stage 4	$(7.81 \pm 0.79) \times 10^{15}$	$(7.18 \pm 0.72) \times 10^{15}$	$(5.35 \pm 0.55) \times 10^{15}$	$(5.17 \pm 0.52) \times 10^{15}$
	Stage 5	$(9.80 \pm 0.99) \times 10^{15}$	$(8.35 \pm 0.84) \times 10^{15}$	$(6.78 \pm 0.70) \times 10^{15}$	$(6.67 \pm 0.68) \times 10^{15}$
5 K CD ₄ + CO	Stage 1	$(3.59 \pm 0.37) \times 10^{15}$	$(3.34 \pm 0.35) \times 10^{15}$	$(3.60 \pm 0.37) \times 10^{15}$	$(3.46 \pm 0.35) \times 10^{15}$
	Stage 2	$(4.22 \pm 0.43) \times 10^{15}$	$(3.94 \pm 0.40) \times 10^{15}$	$(3.83 \pm 0.40) \times 10^{15}$	$(3.62 \pm 0.37) \times 10^{15}$
	Stage 3	$(5.42 \pm 0.55) \times 10^{15}$	$(4.88 \pm 0.49) \times 10^{15}$	$(4.92 \pm 0.50) \times 10^{15}$	$(4.81 \pm 0.48) \times 10^{15}$
	Stage 4	$(5.87 \pm 0.59) \times 10^{15}$	$(5.29 \pm 0.53) \times 10^{15}$	$(5.20 \pm 0.50) \times 10^{15}$	$(4.99 \pm 0.50) \times 10^{15}$
	Stage 5	$(7.44 \pm 0.75) \times 10^{15}$	$(6.35 \pm 0.64) \times 10^{15}$	$(6.73 \pm 0.68) \times 10^{15}$	$(6.55 \pm 0.66) \times 10^{15}$
10 K CH ₄ + CO	Stage 1	$(1.07 \pm 0.11) \times 10^{16}$	$(8.35 \pm 0.84) \times 10^{15}$	$(7.79 \pm 0.79) \times 10^{15}$	$(7.55 \pm 0.76) \times 10^{15}$
	Stage 2	$(1.38 \pm 0.14) \times 10^{16}$	$(1.13 \pm 0.12) \times 10^{16}$	$(8.95 \pm 0.90) \times 10^{15}$	$(8.81 \pm 0.89) \times 10^{15}$
	Stage 3	$(2.82 \pm 0.29) \times 10^{16}$	$(2.40 \pm 0.25) \times 10^{16}$	$(2.12 \pm 0.22) \times 10^{16}$	$(1.90 \pm 0.20) \times 10^{16}$
	Stage 4	$(3.43 \pm 0.35) \times 10^{16}$	$(2.99 \pm 0.30) \times 10^{16}$	$(2.30 \pm 0.24) \times 10^{16}$	$(2.05 \pm 0.21) \times 10^{16}$
	Stage 5	$(3.89 \pm 0.39) \times 10^{16}$	$(3.25 \pm 0.33) \times 10^{16}$	$(2.59 \pm 0.26) \times 10^{16}$	$(2.38 \pm 0.24) \times 10^{16}$
15 K CH ₄ + CO		$(4.01 \pm 0.41) \times 10^{16}$	$(3.09 \pm 0.31) \times 10^{16}$	$(2.76 \pm 0.28) \times 10^{16}$	$(2.50 \pm 0.25) \times 10^{16}$
20 K CH ₄ + CO		$(3.73 \pm 0.38) \times 10^{16}$	$(3.07 \pm 0.31) \times 10^{16}$	$(2.55 \pm 0.26) \times 10^{16}$	$(2.32 \pm 0.24) \times 10^{16}$

Table A10

Concentration of Methyl (CH₃) and Formyl (HCO) Radicals in Methane (CH₄) + Carbon Monoxide (CO) Ice in the Area Containing 90% of Absorbed Electron Energy

Temperature	CH ₃	HCO	Sum
5 K, before rapid radical reactions	$(0.29 \pm 0.03)\%$	$(0.70 \pm 0.07)\%$	$(0.99 \pm 0.10)\%$
10 K, before rapid radical reactions	$(0.16 \pm 0.02)\%$	$(0.90 \pm 0.09)\%$	$(1.06 \pm 0.11)\%$
15 K, end of irradiation	$(0.11 \pm 0.01)\%$	$(0.65 \pm 0.07)\%$	$(0.76 \pm 0.08)\%$
20 K, end of irradiation	$(0.09 \pm 0.01)\%$	$(0.44 \pm 0.04)\%$	$(0.53 \pm 0.06)\%$

Table A11

Contribution Ratios of Rapid Radical–Radical Reactions to the Formation of Ethane (C₂H₆), Acetaldehyde (CH₃CHO), and Formaldehyde (H₂CO) during Electron Processing of Methane (CH₄) + Carbon Monoxide (CO) Ice in Stages 2 and 4

Temperature	Stage	C ₂ H ₆	CH ₃ CHO	H ₂ CO
5 K	stage 2	$(19 \pm 6)\%$	$(63 \pm 15)\%$	$(73 \pm 21)\%$
	stage 4	$(40 \pm 12)\%$	$(72 \pm 21)\%$	$(53 \pm 18)\%$
10 K	stage 2	$(8 \pm 3)\%$	$(28 \pm 10)\%$	$(82 \pm 25)\%$
	stage 4	$(28 \pm 9)\%$	$(75 \pm 22)\%$	$(88 \pm 27)\%$

ORCID iDs

Cheng Zhu  <https://orcid.org/0000-0002-7256-672X>

Alexandre Bergantini  <https://orcid.org/0000-0003-2279-166X>

Ralf I. Kaiser  <https://orcid.org/0000-0002-7233-7206>

References

Abplanalp, M. J., Gozem, S., Krylov, A. I., et al. 2016, *PNAS*, 113, 7727
Ahmadvand, S., Zaari, R. R., & Varganov, S. A. 2014, *ApJ*, 795, 173

Balucani, N., Ceccarelli, C., & Taquet, V. 2015, *MNRAS*, 449, L16
Bennett, C. J., Chen, S.-H., Sun, B.-J., Chang, A. H., & Kaiser, R. I. 2007, *ApJ*, 660, 1588
Bennett, C. J., Jamieson, C. S., Osamura, Y., & Kaiser, R. I. 2005a, *ApJ*, 624, 1097
Bennett, C. J., Jamieson, C. S., Osamura, Y., & Kaiser, R. I. 2006, *ApJ*, 653, 792
Bennett, C. J., & Kaiser, R. I. 2007, *ApJ*, 661, 899
Bennett, C. J., Osamura, Y., Lebar, M. D., & Kaiser, R. I. 2005b, *ApJ*, 634, 698
Bergantini, A., Abplanalp, M. J., Pokhilko, P., et al. 2018, *ApJ*, 860, 108
Bertin, M., Romanzin, C., Doronin, M., et al. 2016, *ApL*, 817, L12
Bludov, M., Khyzhniy, I., Savchenko, E., Sugakov, V., & Uytunov, S. 2020, *NPAE*, 21, 312
Boogert, A. A., Gerakines, P. A., & Whittet, D. C. 2015, *ARA&A*, 53, 541
Bouilloud, M., Fray, N., Benilan, Y., et al. 2015, *MNRAS*, 451, 2145
Brunetto, R., Caniglia, G., Baratta, G., & Palumbo, M. 2008, *ApJ*, 686, 1480
d'Hendecourt, L., Allamandola, L., Baas, F., & Greenberg, J. 1982, *A&A*, 109, L12
d'Hendecourt, L., Allamandola, L., & Greenberg, J. 1985, *A&A*, 152, 130
Dartois, E., Chabot, M., Barkach, T. I., et al. 2019, *A&A*, 627, A55
Dartois, E., Chabot, M., Barkach, T. I., et al. 2021, *A&A*, 647, A177
De Barros, A., da Silveira, E., Pilling, S., et al. 2014, *MNRAS*, 438, 2026
Drouin, D., Couture, A. R., Joly, D., et al. 2007, *Scanning*, 29, 92
Fayolle, E. C., Bertin, M., Romanzin, C., et al. 2011, *ApL*, 739, L36
Fredon, A., Radchenko, A. K., & Cuppen, H. M. 2021, *AcChR*, 54, 745
Frenklach, M., Wang, H., & Rabinowitz, M. J. 1992, *PrECS*, 18, 47
Garrod, R., Park, I. H., Caselli, P., & Herbst, E. 2006, *FaDi*, 133, 51
Geppert, W. D., Hamberg, M., Thomas, R. D., et al. 2006, *FaDi*, 133, 177

- Gerakines, P., Bray, J., Davis, A., & Richey, C. 2005, *ApJ*, **620**, 1140
- Gronkowski, P. 2007, *AN*, **328**, 126
- Gronkowski, P., & Sacharczuk, Z. 2010, *MNRAS*, **408**, 1207
- Gronkowski, P., & Wesolowski, M. 2016, *EM&P*, **119**, 23
- Hartquist, T., & Williams, D. 1990, *MNRAS*, **247**, 343
- He, J., Gao, K., Vidali, G., Bennett, C. J., & Kaiser, R. I. 2010, *ApJ*, **721**, 1656
- Herbst, E. 1991, Methanol in space and in the laboratory in ASP Conf. Ser. Atoms, Ions and Molecules: New Results in Spectral Line Astrophysics, ed. A. D. Haschick & P. T. P. Ho (San Francisco, CA: ASP), **313**
- Herbst, E., & Klemperer, W. 1973, *ApJ*, **185**, 505
- Hernandez, R., Masclat, P., & Mouvier, G. 1977, *JESRP*, **10**, 333
- Hollenberg, J., & Dows, D. A. 1961, *JChPh*, **34**, 1061
- Hollis, J., Remijan, A. J., Jewell, P., & Lovas, F. J. 2006, *ApJ*, **642**, 933
- Hudson, R., & Moore, M. 1999, *Icar*, **140**, 451
- Hudson, R. L., Gerakines, P. A., & Moore, M. 2014, *Icar*, **243**, 148
- Huntress, W., Jr. & Mitchell, G. 1979, *ApJ*, **231**, 456
- Irvine, W. M., Brown, R., Cragg, D., et al. 1988, *ApJL*, **335**, L89
- Irvine, W. M., Friberg, P., Kaifu, N., et al. 1990, *A&A*, **229**, L9
- Ishiguro, M., Kim, Y., Kim, J., et al. 2013, *ApJ*, **778**, 19
- Johnson, R., Pirronello, V., Sundqvist, B., & Donn, B. 1991, *ApJL*, **379**, L75
- Jones, B. M., & Kaiser, R. I. 2013, *JPCL*, **4**, 1965
- Kaiser, R., Eich, G., Gabrysch, A., & Roessler, K. 1997, *ApJ*, **484**, 487
- Kaiser, R. I., Maity, S., & Jones, B. M. 2014, *PCCP*, **16**, 3399
- Kalvāns, J. 2015, *ApJ*, **803**, 52
- Leung, C. M., Herbst, E., & Huebner, W. F. 1984, *ApJS*, **56**, 231
- Maksyutenko, P., Muzangwa, L. G., Jones, B. M., & Kaiser, R. I. 2015, *PCCP*, **17**, 7514
- Matthews, H., Friberg, P., & Irvine, W. M. 1985, *ApJ*, **290**, 609
- Minissale, M., & Dulieu, F. 2014, *JChPh*, **141**, 014304
- Minissale, M., Dulieu, F., Cazaux, S., & Hocuk, S. 2016a, *A&A*, **585**, A24
- Minissale, M., Moudens, A., Baouche, S., Chaabouni, H., & Dulieu, F. 2016b, *MNRAS*, **458**, 2953
- Morton, R. J., & Kaiser, R. I. 2003, *P&SS*, **51**, 365
- Öberg, K. I., Garrod, R. T., Van Dishoeck, E. F., & Linnartz, H. 2009a, *A&A*, **504**, 891
- Öberg, K. I., Linnartz, H., Visser, R., & Van Dishoeck, E. F. 2009b, *ApJ*, **693**, 1209
- Öberg, K. I., Van Dishoeck, E. F., & Linnartz, H. 2009c, *A&A*, **496**, 281
- Pacansky, J., & Dupuis, M. 1982, *JChS*, **104**, 415
- Pantaleone, S., Enrique-Romero, J., Ceccarelli, C., et al. 2020, *ApJ*, **897**, 13
- Petrie, S. 1995, *ApL*, **454**, L165
- Pratap, P., Dickens, J., Snell, R. L., et al. 1997, *ApJ*, **486**, 862
- Quan, D., & Herbst, E. 2007, *A&A*, **474**, 521
- Rank, D., Townes, C., & Welch, W. 1971, *Sci*, **174**, 1083
- Roberts, J., Rawlings, J., Viti, S., & Williams, D. 2007, *MNRAS*, **382**, 733
- Ruiterkamp, R., Charnley, S., Butner, H., et al. 2007, *Ap&SS*, **310**, 181
- Satorre, M., Domingo, M., Millán, C., et al. 2008, *P&SS*, **56**, 1748
- Satorre, M., Millán, C., Molpeceres, G., et al. 2017, *Icar*, **296**, 179
- Savchenko, E., Khyzhniy, I., Uytunov, S., et al. 2019, *NIMPB*, **460**, 244
- Savchenko, E., Khyzhniy, I., Uytunov, S., Bludov, M., & Bondybey, V. 2020, *NIMPB*, **469**, 37
- Schutte, W., & Greenberg, J. 1991, *A&A*, **244**, 190
- Smith, I. W., Herbst, E., & Chang, Q. 2004, *MNRAS*, **350**, 323
- Snelson, A. 1970, *JPhCh*, **74**, 537
- Socrates, G. 2004, Infrared and Raman Characteristic group Frequencies (3rd ed.; New York: Wiley)
- Soma, T., Sakai, N., Watanabe, Y., & Yamamoto, S. 2018, *ApJ*, **854**, 116
- Teolis, B., Loeffler, M., Raut, U., Famá, M., & Baragiola, R. 2007, *Icar*, **190**, 274
- Tielens, A., & Hagen, W. 1982, *A&A*, **114**, 245
- Turner, A. M., Abplanalp, M. J., Chen, S. Y., et al. 2015, *PCCP*, **17**, 27281
- Turner, A. M., Bergantini, A., Abplanalp, M. J., et al. 2018, *NatCo*, **9**, 1
- Turner, B., Terzieva, R., & Herbst, E. 1999, *ApJ*, **518**, 699
- Vasyunin, A., & Herbst, E. 2013, *ApJ*, **769**, 34
- Vasyunina, T., Vasyunin, A., Herbst, E., et al. 2013, *ApJ*, **780**, 85
- Willacy, K., & Millar, T. 1998, *MNRAS*, **298**, 562
- Wormhoudt, J., & McCurdy, K. 1989, *CPL*, **156**, 47
- Yeghikyan, A. 2011, *Ap*, **54**, 87